ORIGINAL ARTICLE

An experimental and finite element investigation of chip separation criteria in metal cutting process

Junli Li[1] · Ziru Huang[1] · Gang Liu[1] · Qinglong An[2] · Ming Chen[2]

Abstract

Chip separation is an important issue in finite element method (FEM)-based simulation of the cutting process owing to its significant impact on the predicted chip formation, as well as on the temperature and stress distributions. Typically, the chip separation criteria and the arbitrary Lagrangian–Eulerian (ALE) method have been utilized in chip formation simulations. This study aimed to evaluate the chip separation criterion and the ALE method in terms of chip formation, cutting force, cutting temperature, and stress distribution. Particularly, the effective plastic strain criterion and the failure-zone-assisted and ALE methods were utilized to model the orthogonal cutting of Inconel 718 alloy. Furthermore, experimentations were performed, and the results of FEM predictions were compared with the experimentally measured results. In general, ALE method was more consistent with the experiment. The ESPC method does not seem to handle chip shape and cutting temperature well, while the FZA method may not be suitable for predicting surface stress due to the deformation and failure of the material concentrated in the fail assist area.

1 Introduction

In the past few decades, a large number of studies have been performed to obtain a better understanding of machining processes. Traditionally, this goal has been achieved by using experimental and analytical methods. However, high cost and extremely complex cutting processes involving thermo-mechanical effects have become the primary obstacles in the development and application of the two aforementioned methods [1]. The finite element method (FEM) has been widely used since the 1980s, benefiting from the advancements in computational efficiency and speed. The FEM is a useful tool for the analysis of metal cutting processes because it can

incorporate the effects of strain, strain rate, and temperature, as well as complicated frictional behaviors [2] [3].

However, the difficulties with FEM application, including the material constitutive model, tool–chip interface friction, and chip separation from the workpiece, are obvious [4]. Among these difficulties, chip separation is an important issue in FEM modeling owing to its significant impact on chip formation, stress, and temperature predictions. Typically, chip separation method based on separation criterion and the arbitrary Lagrangian–Eulerian (ALE) method are usually used in the simulation of cutting processes. Unlike the chip separation criterion, wherein a special critical value of the geometry or a physical property is used, the ALE method considers the chip formation process as an automatic material flow [5].

In the early finite element (FE) model, a chip separation criterion was typically used to assist in the chip separation from a workpiece. Hitherto, many chip separation criteria are used in FE modeling, such as the distance, effective plastic strain, strain energy density, and normal failure stress [6]. Ortiz-de-Zarate et al. [7] introduced a ductile failure model to represent the chip segmentation phenomena observed in machining of titanium alloy Ti64 at low cutting speeds. Tiffe et al. [8] proposed two different damage models to analyze chip formation mechanism

✉ Gang Liu
liugang@sues.edu.cn

[1] School of Mechanical Engineering, Shanghai University of Engineering Science, Shanghai 201620, People's Republic of China

[2] School of Mechanical Engineering, Shanghai Jiao Tong University, Shanghai 200240, People's Republic of China

of hardened steel. One is a ductile damage parameter calculated as the accumulation of a normalized fracture strain; the other is Cockroft–Latham model which is based on the maximum principal stress. However, both of the models cannot predict the damage realistically. In order to simulate chip formation, Johnson–Cook fracture model, which was based on equivalent plastic strain, was employed as a criterion at the onset of damage [9]. Johnson–Cook fracture model was also found in Du et al.'s [10] and Huang et al.'s [11] works. Chen et al. [12] used different plastic constitutive models, Johnson–Cook (JC) model, JCM model, and KHL models to simulate the segmented chip formation in Ti-6Al-4V alloy orthogonal cutting. The JC damage initiation and energy-density-based damage evolution criteria were applied in cutting simulation. For most conditions, the predicted forces and chip morphology agree well with the experimental results. The separation of the chip from the workpiece was modeled using a predefined failure zone, where the failure occurred at a critical accumulated equivalent inelastic deformation [13]. Zhang [14] evaluated several separation criteria and concluded that none of the single separation criteria can be used reliably as a complete separation criterion in the FEM simulation of an orthogonal metal cutting process. Rosa et al. [15, 16] provided a combined numerical modeling performed by means of an updated Lagrangian approach and ductile damage begins to accumulate, eventually leading to separation at the tool tip. Their results demonstrated that material separation is caused by shearing rather than tension.

The arbitrary Lagrangian–Eulerian (ALE) method combines the features of pure Lagrangian analysis, in which the mesh follows with the material, and Eulerian analysis, in which the mesh is fixed spatially and the material flows through the mesh. Saez-de-Buruaga et al. [17] developed a coupled Eulerian–Lagrangian (CEL) finite element model with the Johnson–Cook (JC) plasticity model to predict the influence that ferrite pearlite steel variants have on fundamental process variables and tool wear. Arrazola et al. [18] employed two distinct FE models with ALE fully coupled thermal-stress analyses to study not only the effects of FE modeling with ALE method but also to investigate the influence of limiting shear stress at the tool–chip contact on frictional conditions. Ducobu et al. [19] presented a CEL method to model the chip formation in AA2024-T3. A 2D plane strain orthogonal cutting CEL model with JC material behavior and Bao–Wierzbicki model to describe the behavior of the machined material has been introduced. Issa et al. [20] propose an adaptive numerical methodology to simulate 2D machining processes taking into account the main thermo-mechanical phenomena such as the nonlinear isotropic and kinematic hardening with thermal and ductile damage effects. Zhang et al. [21] evaluated two sets of JC model parameters for Ti-6A-4V evaluated, using three types of metal cutting models. These models are based on three different formulations: Lagrangian, ALE, and CEL.

To take into account the recrystallization phenomenon, a new material constitutive model denoted "multi-branch" (MB) model was developed by Yameogo et al. [22]. Their researches showed that the MB model is more suitable for high-speed machining. A "metallurgy-based" constitutive model, taking into account a dynamic recrystallization process, is identified in Courbon et al.'s [23] work. It clearly leads to a better description of the thermo-mechanical behavior than the commonly used JC model. Nasr et al. [24] presented an ALE FE model to simulate the effects of tool edge radius on residual stresses when dry turning AISI 316L stainless steel. The usage of Eulerian formulation avoids the necessity to define the failure criterion for chip formation. Ozel et al. [25] presented a comparison of 3D machining models developed using commercially available FE softwares ABAQUS/Explicit and DEFORM™ 3D Machining. Chip formation was modeled with ALE formulation. The purpose of such comparison is to provide a candid demonstration about the capabilities and predictions obtained using the commercially available FE modeling software.

However, from the literature review of cutting simulations, a comparison between the chip separation criterion has not been reported yet. Inconel 718 is often used in aerospace, power, and biomedical applications due to its high tensile strength, resistance to corrosion, and high temperatures [26]. The purpose of this study is to investigate the differences of ALE method and chip separation criterion in chip formation, stress distribution, temperature, and cutting force prediction during simulation of orthogonal cutting of Inconel 718. A comparison between the results of the experimental measurement and those of the FEM predictions was also performed to validate the simulations.

2 Experimental setup

The turning experiments on Inconel 718 alloy were performed on an INDEX G200 turn-mill center. Inconel 718 has a maximum yield strength of 988 MPa. The metallographic diagram
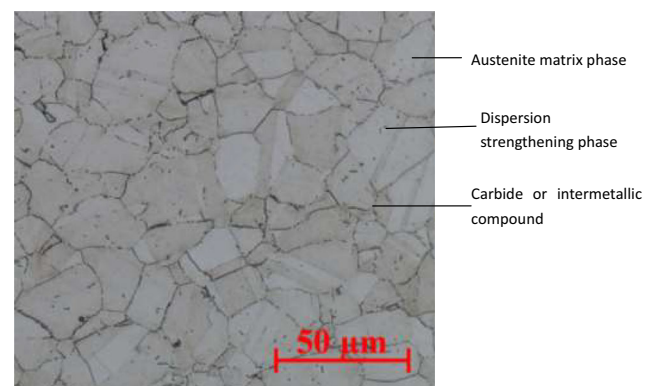

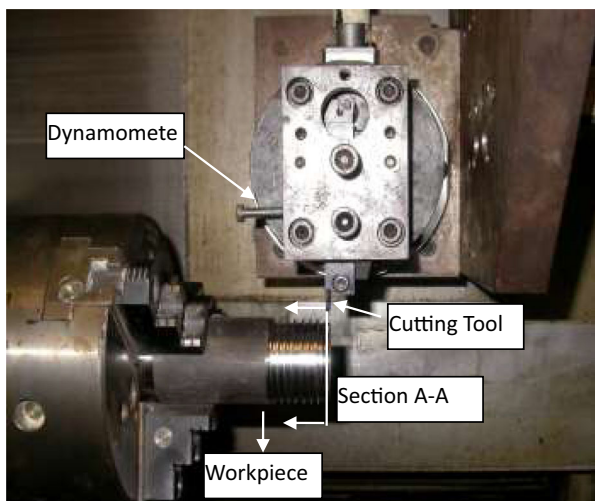**Fig. 1** Metallographic structure of Inconel 718

Fig. 2 Setup of the turning experiment

of Inconel 718 is as follows (Fig. 1). The main component is a single austenite matrix phase. The austenite matrix phase also contains a large number of dispersed phases. To strengthen the phase, there are many carbides or intermetallics on the grain boundaries of the alloy. In the compound phase, these carbides precipitate out and grow up at grain boundaries, and their shape is similar to discontinuous near-spherical particles.

The experimental setup is shown in Fig. 2. An uncoated commercial carbide insert was used under a dry condition. The tool cutting edge inclination angle was 0°, the rake angle was 0°, and the clearance angle was 5°. The edge radius of the cutting tool is 15 μm. Further information about the cutting tool and the workpiece is shown in Table 1. The cutting forces were measured by a Kistler 9272 piezoelectricity dynamometer. Figure 2 shows metallographic structure of Inconel 718.

In addition, high-speed photography was used to observe the experimental cutting process. The cutting parameters and the primary chemical components of Inconel 718 alloy are shown in Tables 2 and 3, respectively. The chip morphology was analyzed by using a Philips XL30-FEG scanning electronic microscope (SEM). The stress in the depth of the machined surface was measured by using an X350A X-ray diffraction system in the experiments.

Table 2 Cutting parameters used in the turning experiments on Inconel 718 alloy

	1	2	3	4	5
Feed rate (f) (mm/rev)	0.15	0.15	0.15	0.15	0.15
Cutting speed (v) (m/min)	15	35	55	70	90
Depth of cut (*doc*) (mm)	1	1	1	1	1

3 Numerical model

3.1 Material modeling

The JC material model was utilized wherein the flow stress was dependent on the strain, strain rate, and temperature. This model is suitable for modeling cases with high strain, high strain rate, high strain hardening, and nonlinear material properties, which represent the main numerical challenges of metal cutting modeling. Additionally, it has been widely used in modeling cutting processes and has proven its suitability [15]. The following JC equation was utilized:

$$\sigma = \left[A + B\left(\varepsilon^{pl}\right)^n\right]\left[1 + CIn\left(\frac{\dot{\varepsilon}^{pl}}{\dot{\varepsilon}_0}\right)\right]\left(1 - \widehat{\theta}^m\right) \tag{1}$$

where σ is the material flow stress (MPa), ε^{pl} the equivalent plastic strain, $\dot{\varepsilon}^{pl}$ the equivalent plastic strain rate, $\dot{\varepsilon}_0$ the reference plastic strain rate, n is the strain hardening index, A–C and m are the material parameters, and $\widehat{\theta}$ is the nondimensional temperature given by

$$\widehat{\theta} = \begin{cases} 0 & \text{for } \theta < \theta_t \\ \dfrac{\theta - \theta_t}{\theta_m - \theta_t} & \text{for } \theta_t \leq \theta \leq \theta_m \\ 1 & \text{for } \theta > \theta_m \end{cases} \tag{2}$$

where θ is the current temperature, θ_m is the melting temperature, and θ_t is the transition temperature, below which temperature dependence does not exist. The physical

Table 1 Physical properties of Inconel 718 alloy and cutting tool [26]

Property	Inconel 718	Tool
Modulus of elasticity (GPa)	201 (20 °C), 192 (200 °C), 185 (400 °C), 173 (600 °C), 154 (800 °C)	615
Poisson's ratio	0.3	0.22
Density (kg/m³)	8190	14,900
Specific heat capacity (J/kg °C)	451 (20 °C), 482 (200 °C), 494 (400 °C), 539 (600 °C), 615 (800 °C), 707 (900 °C)	138
Thermal conductivity (W/m °C)	13.4 (20 °C), 15.9 (200 °C), 18.3 (400 °C), 21.2 (600 °C), 23.6 (800 °C), 30.4 (900 °C)	79
Melting temperature (°C)	1573 °C	
Linear coefficient of thermal expansion (mm/mm °C)	13.1×10^{-6} (20 °C), 13.8×10^{-6} (200 °C), 14.7×10^{-6} (400 °C), 15.3×10^{-6} (600 °C), 17.1×10^{-6} (600 °C)	

Table 3 Chemical components of Inconel 718 alloy used in the experiments

	Ni	Cr	Al	Ti	Fe	Other
Inconel 718	30.0–55.0	17.0–21.0	0.2–0.6	0.65–1.15	15.0–21.0	Nb: 4.75–5.5

properties of the workpiece and the tool material, and the JC parameters for Inconel 718 alloy are given in Tables 3 and 4, respectively.

3.2 Finite element mesh control and boundary conditions

A plane strain FE model was built using ABAQUS/ Explicit 6.14-1 to simulate orthogonal dry cutting of Inconel 718 with continuous chips. Coupled temperature displacement analysis was used in step to allow for temperature-dependent properties and heat transfer. The workpiece and the tool consisted of combined temperature displacement four-node bilinear elements in the current simulations. The effective rake angle and effective clearance angle were set to 0° and 5°, respectively, according to the insert geometry and installation plane.

A typical refined mesh for the ALE method in the high deformation areas, and on the slave (chip) and master (tool) surfaces, used the initial geometry, as shown in Fig. 3. An FEM simulation model with ALE scheme with pure Lagrangian boundaries is designed. For the 0.15-mm feed, the workpiece consisted of 6526 nodes and 6362 elements, and the tool consisted of 356 nodes and 314 elements. The number of nodes and elements in the different zones of the workpiece depends on the deformation degree. In general, the primary deformation zone has a finer mesh than that of the other zones.

For the thermal boundary conditions, the temperatures of the workpiece and the tool were initially set to 20 °C. Heat transfer could take place between the workpiece and the tool. Moreover, heat transfer by convection was allowed along the free sides of the tool and the chip, whereas heat transfer by conduction was applied at the tool–chip interface. The bottom of the workpiece was not allowed to move in the Y-direction as both the left and the right mesh of the workpiece were constrained, and, therefore, the material could only flow from left to right. The tool was fully constrained in both the X- and the Y-directions.

3.3 Chip separation

Herein, the effective plastic strain criterion (EPSC) and the failure-zone-assisted (FZA) and ALE method were used in modeling the chip formation to evaluate their impacts on the cutting process. The Lagrangian formulation, which can simulate both the steady and the unsteady chip formation processes, was used in both the EPSC and the FZA models.

In the ALE method, the material flows around the tool tip like a liquid. In other words, there is no need to define the failure criterion of chip separation due to the automatic chip formation caused by the continuous plastic flow of materials near the tool. Specially, the workpiece was considered as a tube with one entrance and two exits, and the workpiece material flowed from left to right (as shown in Fig. 3). At the defined Eulerian boundaries, the material entered the workpiece from the left-hand boundary and exited through the right-hand boundary. The top surface of the chip was defined as Lagrangian boundaries. To retain the Eulerian boundaries, we imposed adaptive mesh constraints on both the left and the right sides of the workpiece in the X-direction and on the top area of the chip in the Y-direction. Additionally, at the surfaces without any constraint, the mesh moved with the material (Lagrangian formulation) such that the initial chip shape was free to evolve into whatever shape was necessary to satisfy the current conditions [5]. In the current ALE model, the tool did not move. It was constrained in both the X- and the Y-directions.

The EPSC result showed better agreement with the experiment result compared to those of the other methods in Zhang's [14] research, and it was adopted as one of the three typical methods in the current study. In particular, the element-based effective plastic strain failure criterion was employed in this study. The damaging parameter w is defined in the following equation:

$$w = \left(\overline{\varepsilon}_0^{pl} + \sum \Delta \overline{\varepsilon}^{pl} \right) / \overline{\varepsilon}_f^{pl} \qquad (3)$$

where $\overline{\varepsilon}_0^{pl}$ is the initial equivalent plastic strain value, $\Delta \overline{\varepsilon}_0^{pl}$ is the equivalent plastic strain increment of every increment step, and $\overline{\varepsilon}_f^{pl}$ is the failure strain. The elements fail when the damage parameter w exceeds 1. When the failure criterion meets at the integration points, all the stress components of the failure elements between the undeformed chip layer and the
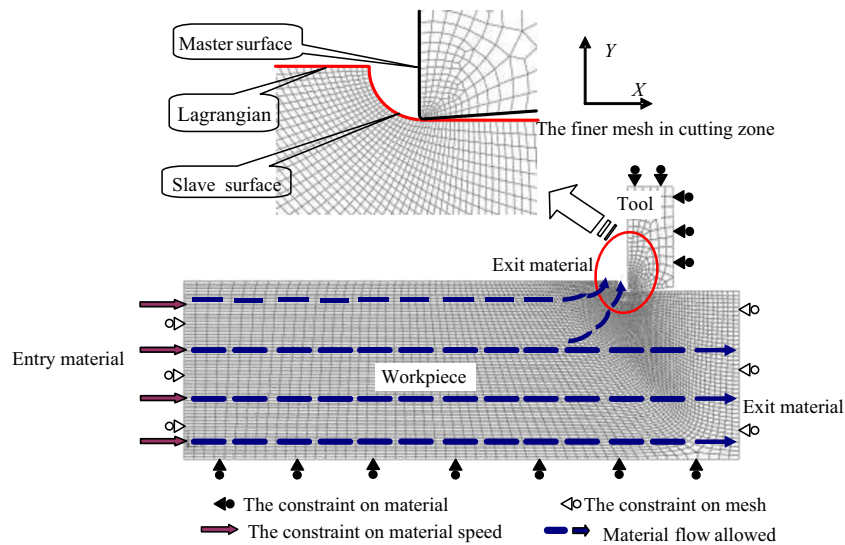
Table 4 JC parameters for Inconel 718 alloy by Sievert and Noack [26]

A (MPa)	B (MPa)	N	C	ε_0	m
450	1700	0.65	0.017	1	1.3

Fig. 3 Initial mesh configuration and boundary conditions of the workpiece and tool as used by the ALE method

basic part will be set to zero and deleted from the calculation circle. In this paper, JC failure model corresponding to JC constitutive model is adopted, shown as follows:

$$\overline{\varepsilon}_f^{pl} = [D_1 + D_2\exp(D_3\sigma)]\left[1 + D_4 In\dot{\varepsilon}\right][1 + D_5 InT] \quad (4)$$

where σ, $\dot{\varepsilon}$, and T are the stress, strain rate, and temperature, respectively, and D_1, D_2, D_3, D_4, and D_5 are material-dependent fracture constants, as shown in Table 5

Figure 4 illustrates the FZA model with a predefined cutting routine. As shown in the figure, the workpiece consists of three parts: the undeformed chip layer, the failure zone, and the basic part. The undeformed chip layer was designed to be a parallelogram because, with an oblique mesh, a chip can be more easily formed along the tool rake face, and to prevent the appearance of element distortion. Additionally, the length and the width of the parallelogram mesh should be set below 10 µm owing to the high shear localization. Here, the two values were 8 µm in the undeformed chip layer. Four-node bilinear coupled temperature displacement quadrilateral elements were used in both the workpiece and the tool mesh.

In the FZA method, the separation of the chip from the workpiece was modeled using a failure zone, as shown in Fig. 4. The failure in this zone occurred when the accumulated equivalent inelastic deformation reached a critical value. Consequently, the mesh elements in this zone were deleted and the cutting tool was moved.

3.4 Modified Coulomb friction model

The contact behavior between the chip and the tool is significant owing to its direct effect on the tool performance and chip formation. However, it is difficult to evaluate the tool–chip interaction experimentally because of the high

temperature, high temperature gradient, as well as the high strain and strain rate in the very small region. Many attempts have been performed to understand the frictional behavior at the tool–chip interface. In the present study, the Coulomb friction model with variable friction coefficient is used for contact problems with friction, and is written as:

$$\left\|\overrightarrow{F}_T\right\| \leq \eta\left\|\overrightarrow{F}_N\right\| \quad (5)$$

where η is the friction coefficient, which is the ratio of the norm of the tangential force $\overrightarrow{F}_T$ to the normal force $\overrightarrow{F}_N$ at any contact point of the contact interface. Following the works by [48–50], the friction parameter η usually taken as constant is taken here function of the local temperature T and the local sliding velocity $\|V_g\| = \|\overline{V}_g\|$ at the contact point according to:

$$\eta = \left[\eta_\infty + (\eta_0 - \eta_\infty)e^{-\gamma V_g}\right]\left[1 - \left(\frac{T}{T_m}\right)^q\right] \quad (6)$$

where η_∞ describes the friction coefficient at high (or infinite) sliding velocity, η_0 the friction coefficient at low sliding velocity, $\|V_g\| = \|\overline{V}_g\|$ the sliding velocity, T the interface temperature, T_m the lowest melting temperature between materials in contact; γ a parameter describing the sensitivity to the sliding velocity, and q a parameter describing the sensitivity to the temperature.

Table 5 Johnson–Cook damage parameters of Inconel 718 [27]

D_1	D_2	D_3	D_4	D_5
0.04	0.75	−1.45	0.04	0.89

Fig. 4 Mesh configuration and boundary conditions of the failure zone model
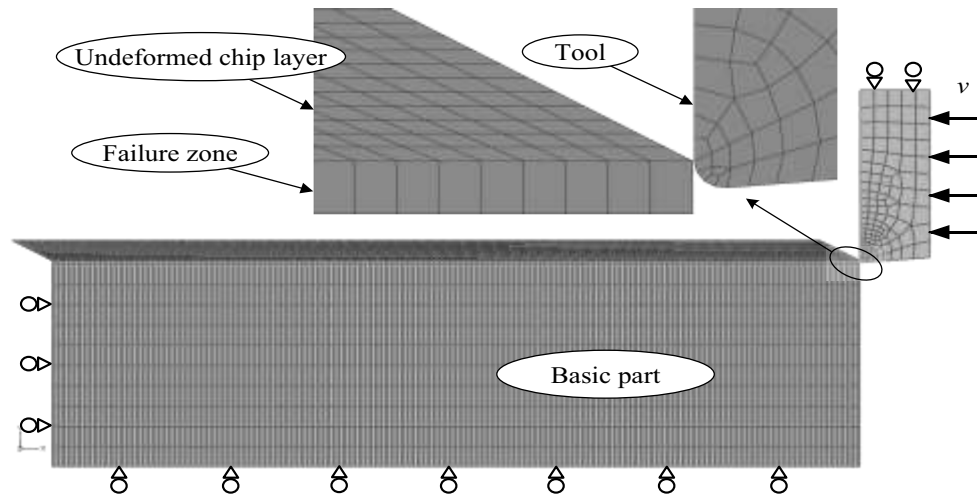
3.5 Heat generation

Heat generation during metal cutting is important in tool wear and is critical in surface integrity and chip formation. The majority of the heat arises from plastic deformation and friction. The temperature increment associated with the heat generation may be expressed by:

$$\Delta T = \frac{f_1 \cdot f_2 \cdot \overline{\sigma} \cdot \partial \overline{\varepsilon}^{pl}}{\rho C_p} \quad (7)$$

where ΔT is the temperature increment; f_1 and f_2 are the work-heat convection factor and the conversion efficiency factor, respectively (both f_1 and f_2 were set to 0.9 as most of the workpiece deformation is converted into thermal energy); $\overline{\sigma}$ is the effective stress; $\partial \overline{\varepsilon}^{pl}$ is the effective plastic strain increment; and ρ and C_p are the material density and specific heat, respectively.

The thermal dissipation arising from the Clausius–Duhem inequality is given by Issa et al. [20]:

$$\phi^{th} = -\frac{\overrightarrow{q}}{T} \cdot g \geq 0 \quad (8)$$

Note that $\overrightarrow{g} = g\overrightarrow{r}ad(T)$ is known as soon as the temperature is known, the heat flux vector $\overrightarrow{q}$ can be derived from the Fourier potential in the framework of the linear heat theory and leads to:

$$\overrightarrow{q} = -k\overrightarrow{g} \quad (9)$$

where k is the heat conduction coefficient of the thermally isotropic material. By combining this equation together with the energy balance (or the first law of thermodynamic) the following generalized heat equation can be obtained:

$$div\left(kg\overrightarrow{r}adT\right) + \phi^M - \rho C_v \dot{T} + T\left[\frac{\partial \sigma}{\partial T} : \dot{\overline{\varepsilon}}^e + \frac{\partial X}{\partial T} : \dot{\alpha} + \frac{\partial R}{\partial T} \dot{r} - \frac{\partial Y}{\partial T}\dot{D}\right] = 0 \quad (10)$$

This partial differential equation together with appropriate boundary conditions will be used to derive the weak variational functional associated with the thermal problem.

4 Results and discussions

4.1 Chip formation

The chip formation process is presented in Fig. 5. As shown in the figure, similar chip morphology and stress distribution were produced in the ALE and FZA models, whereas the chip morphology modeled by the EPSC method was slightly different. Furthermore, cracks occurred at the bottom of the EPSC chip because of the removal of the failure elements. Meanwhile, due to the removal of failure elements, the machined surface in the EPSC model is not as smooth as the surface modeled by the ALE and FZA methods.

In addition, the chip curve radius obtained by the three methods was also investigated. Figure 5a and b show that the ALE and FZA methods obtained nearly the same chip curve radius. In contrast, the chip curve radius obtained by the EPSC method was much smaller, which could be attributed to the effect of shear angle, as shown in Eq. (11), Shaw et al. [1]:

$$\tan \phi_n = \frac{(t/t_c)\cos \alpha_n}{1 - (t/t_c)\sin \alpha_n} \quad (11)$$

where Φ_n is the normal shear angle, α_n the normal rake angle, and t and t_C are the undeformed chip thickness and chip thickness, respectively. In the present study, α_n and t were
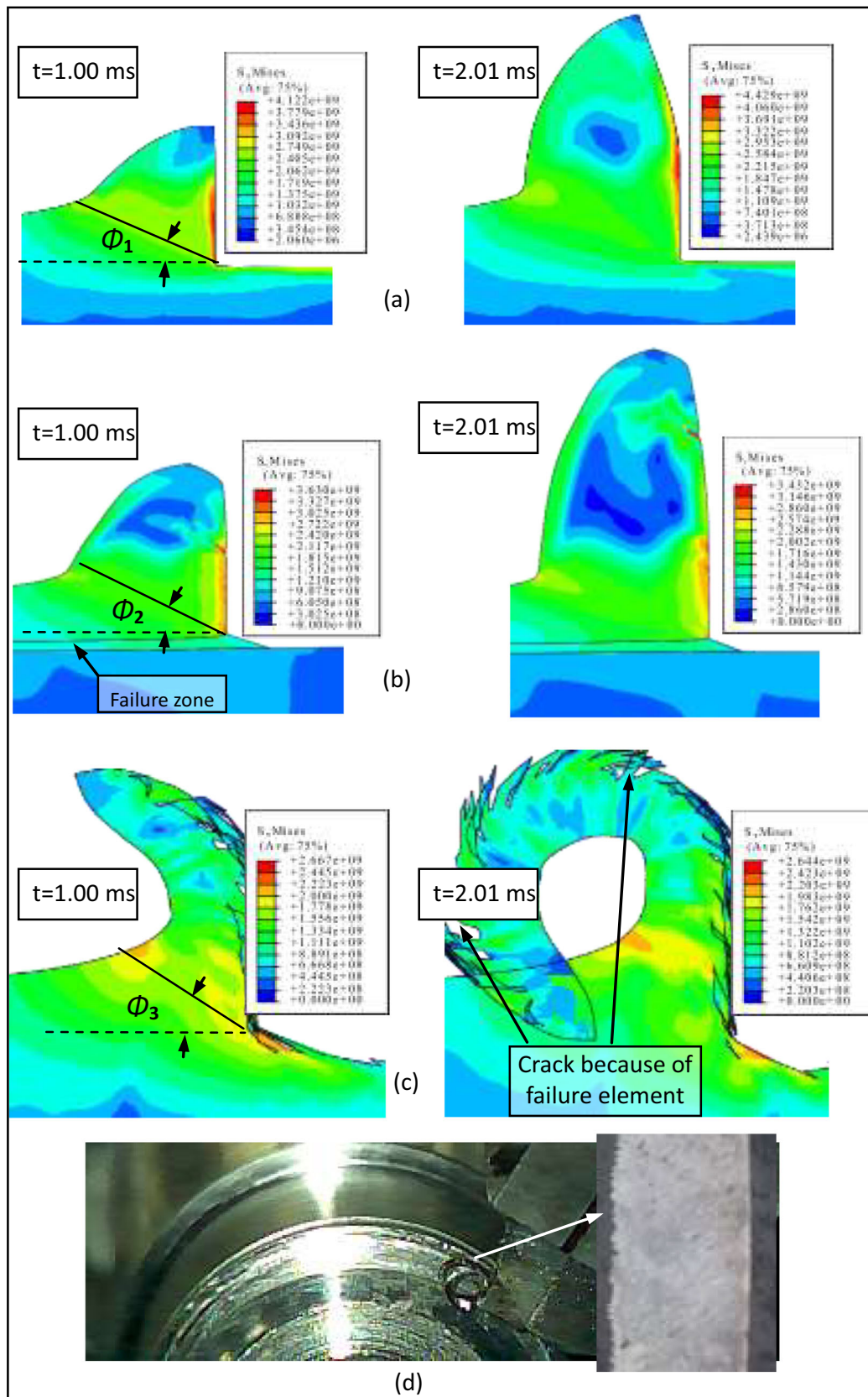
Fig. 5 Chip formation process for the three FE methods and the experiment: **a** ALE, **b** FZA, **c** EPSC, and **d** experimental; cutting conditions: cutting speed = 70 m/min, *doc* = 1 mm, feed rate = 0.15 mm/rev

constant such that Φ_n was determined by t_C. Specifically, Φ_n will increase with decreasing t_C from Eq. (7). Meanwhile, it is obvious that the chip length of the EPSC model was much longer than that of the first two models. Hence, the chip thickness of the EPSC model was smaller when the chip volume was invariable.

With a larger shear angle Φ_n and a smaller chip thickness, it appears that the chip of the EPSC model was more likely to bend. It should be noted that the same experimental results can be obtained with the same tools and cutting conditions. Due to different material separation methods, these three simulation methods will produce different chip thicknesses and curve radius. This is the significance of this research, that is, to evaluate the impact of chip separation rules on the simulation of machining processes.

Figure 6 presents the experimental chip imaged from the SEM after erosion and the chips modeled by the different chip formation techniques. Although continuous chips were produced in both the experiments and the simulations, the morphology and the thickness of these chips were different. The chip thickness was determined by averaging five measurements from the chip top to the chip bottom (as shown in Fig. 6). It is worth noting that, although the chip thicknesses of the four methods did not agree well with each other, they still yielded the same trend in that
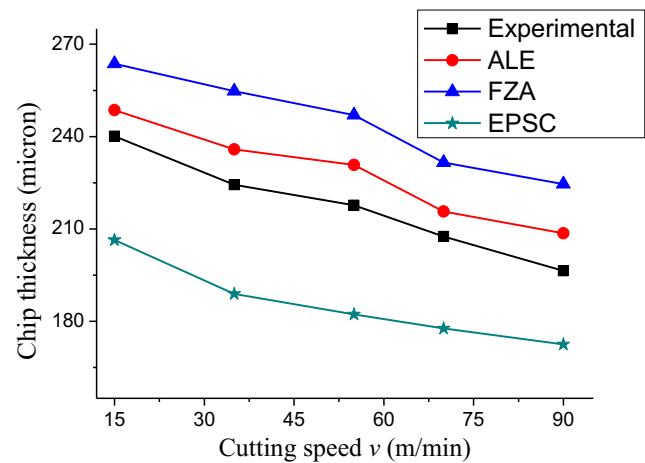

Fig. 7 Chip thickness obtained by the FEM and experimental measurement at different cutting speeds

the chip thickness decreased with increasing cutting speed (as shown in Fig. 7).

In particular, it is worth noting that the chip thickness obtained by the ALE method was more consistent with the experimentally measured thickness than those obtained by the other methods. In contrast, the chip thickness obtained by the FZA method was overestimated, whereas that obtained by the EPSC method was underestimated, which could be attributed
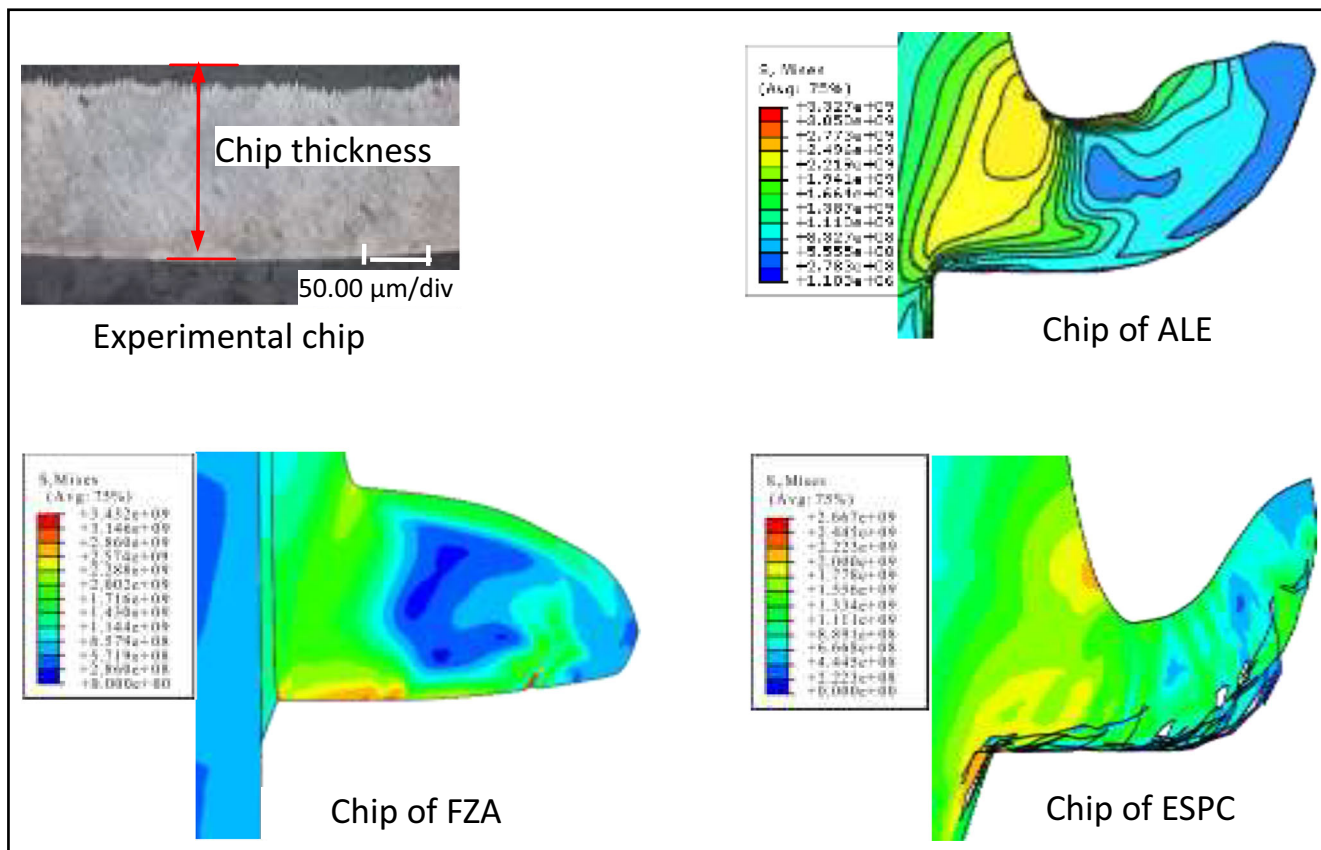

Fig. 6 Chips predicted by the experimental measurement and FEM under the following cutting conditions: $doc = 1$ mm, $f = 0.15$ mm/r, $v = 70$ m/min

to the individual use of the material failure model. Specifically, in the FZA model, because a failure was only considered for the material in the pre-assumed failure zone, the elements beyond the failure zone could deform freely during the cutting process, which finally resulted in a larger chip thickness. The failure elements were removed from the chip and the workpiece in the EPSC model; therefore, many cracks occurred in both the bottom of the chip and the top of the workpiece, which finally resulted in a smaller chip thickness.

4.2 Cutting force

The predicted and measured cutting and the thrust forces for five cutting speeds from 15 to 90 m/min are shown in Fig. 8. According to Fig. 8a, it is clear that the cutting force of the four methods yielded almost a similar pattern in that the force magnitude decreased with increasing cutting speed. Additionally, it is clear that the cutting force predicted by the ALE and EPSC methods was closer to the experimentally measured force, whereas that predicted by the FZA method was much smaller. Furthermore, the cutting force predicted by the ALE method was larger than those predicted by the other methods.

In the ALE model, no material damage law was used, and the chip was formed by the automatic material movement. The region near the cutting tool was assumed to be an Eulerian fluid area. The fluid material experienced thorough deformation during the cutting process, which could lead to an increasing cutting force compared with those of the other methods. Meanwhile, although the EPSC and FZA methods had a smaller cutting force than that of the experimental measurement, the EPSC method had a much better performance than that of the FZA method in predicting the cutting force. A comparison of the cutting forces showed that the force value of the FZA method was underestimated. In the simulation process of the FZA method, only the material in the failure zone was considered for damage; the uncut chip layer turned into a chip when the damage law of these material elements was satisfied. The chip

formation in the FZA method had no relationship with the uncut chip layer but had one with the failure zone, which caused a distortion of the predicted cutting force.

Figure 8b shows the thrust force results produced by the four methods. Different from cutting force, the thrust force generated by the four methods has different trends. In particular, the experimental measurement, ALE and FZA methods have the same trend: the thrust decreases with the increase of cutting speed. However, the thrust force produced by the ALE and FZA methods decreased slowly with the increase in cutting speed, which shows that the friction coefficient changes with the cutting speed in the experiment. In the FE model, such dependency is not present yet. In contrast, the thrust force produced by the EPSC method had the opposite tendency. The tendency of the thrust force produced by the EPSC method changed as the cutting speed increased. Initially, the thrust force decreased from 387 to 341 N when the cutting speed increased from 15 to 35 m/min; when the cutting speed increased from 35 to 75 m/min, the thrust force also increased from 341 to 365 N; finally, the thrust force increased to 375 N when the cutting speed increased to 90 m/min. It is obvious that, whether it was the force magnitude or the trend, the result of the ALE method matched best with the experiment result.

In the literature review, a similar conclusion was obtained by Haglund et al. [5]. Their studies indicated that, if the agreement with the cutting force was good, then the thrust force was underestimated, whereas if the thrust force agreed well, then the cutting force was overestimated. In general, an exact match between the FEM and the experimental results could not be expected because of the different sources of errors in each of them. The primary source of errors encountered in the FEM modeling could be attributed to the material modeling, numerical integration, and interpolation, and assumed friction condition by Nasr et al. [24].

Furthermore, a simulation was run with a constant tool edge radius, even though, practically, the tool edge might wear out or become damaged during cutting. Meanwhile,
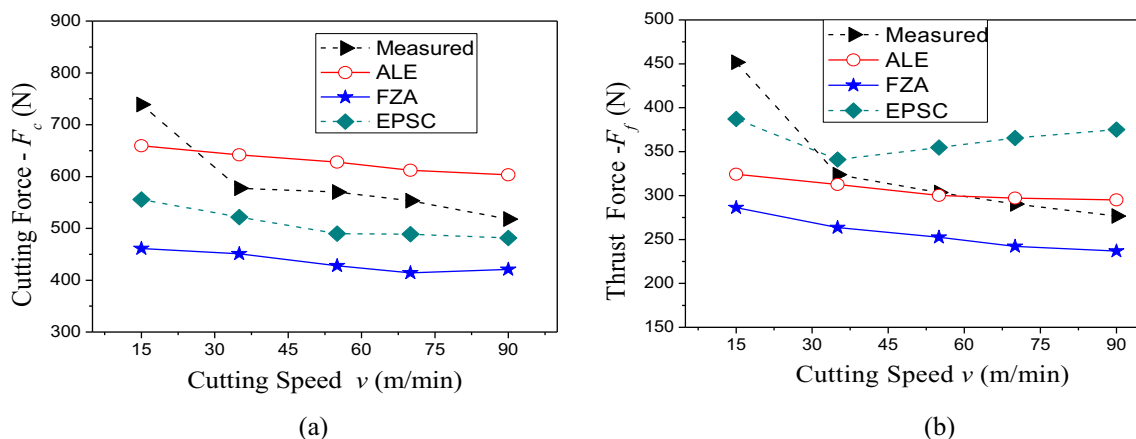

(a)　　　　　　　　　　　　　　　　　　　　　　(b)

Fig. 8 Force results of the FEM and experimental measurement at different cutting speeds. **a** Cutting force. **b** Thrust force

the primary sources of errors in the experimental results were those encountered in the force measurement. Additionally, the actual workpiece material was not 100% homogeneous, whereas it was considered to be a purely homogeneous material in the FEM simulation.
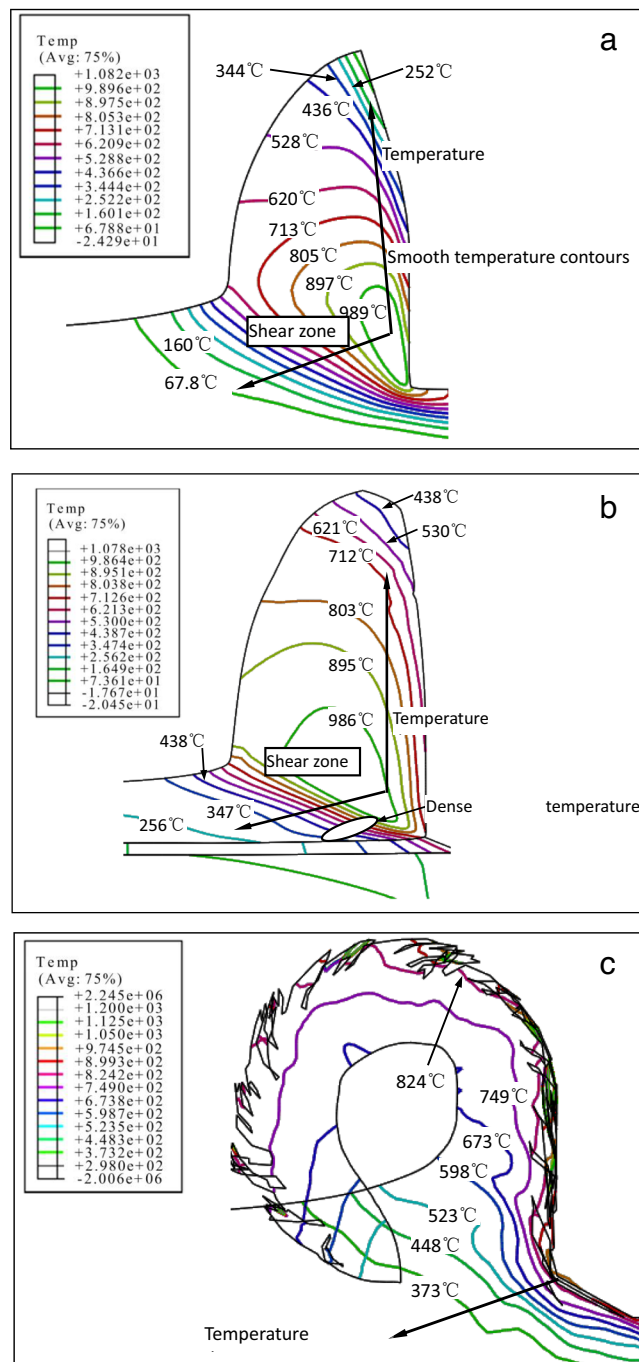

Fig. 9 **a** Temperature distribution predicted by ALE under the following cutting conditions: v = 70 m/min, f = 0.15 mm/rev, doc = 1 mm. **b** Temperature distribution predicted by FZA under the following cutting conditions: v = 70 m/min, f = 0.15 mm/rev, doc = 1 mm. **c** Temperature distribution predicted by the EPSC method under the following cutting conditions: v = 70 m/min, f = 0.15 mm/rev, doc = 1 mm

4.3 Temperature distribution

Figure 9 shows the temperature distribution in the chip and the workpiece for the (a) ALE model, (b) FZA model, and (c) EPSC model. Although similar distributions and almost identical temperature amplitudes were obtained in the ALE and FZA models, there are still some differences between them. First, the temperature predicted by the ALE method in the primary deformation zone was about 50 °C higher than that predicted by the FZA method. Next, it showed that the ALE method produced more intensive temperature contour lines in the primary and secondary deformation zones. Finally, the highest temperature was more adjacent to the tool rake face in the ALE model.

Figure 9c shows the temperature distribution predicted by the EPSC method. It is obvious that not only the chip morphology but also the temperature distribution was distinctly characterized by the EPSC method. As shown in the Fig. 9c, a much higher temperature was generated because of the excessive element distortion. Meanwhile, it could be found that the temperature in the primary deformation zone was lower than those generated by the other two methods. In addition, the temperature contour lines were relatively sparse.

Furthermore, the temperatures produced by the three FE methods were different. Generally, except for the contour density, the ALE method and the FZA method have almost the same temperature distribution. As shown in Fig. 9a and b, the temperature predicted by the ALE and FZA methods decreased apart from the shear zone. It is well known that the cutting heat primarily comes from the energy of the deformation in the shear zone and from the friction along the tool–chip interface. The temperature produced by the ALE and FZA methods indicates that shear deformation had a greater impact on the thermal increment than that of friction. However, the ALE method had smoother temperature contours because of the automatic material fluid.

Compared with the chip separation method described above, in addition to the knife–chip interface, the ESPC method has a different temperature distribution, and its temperature drop position is also different. As the temperature rises due to material deformation and chip friction, it seems that in the ESPC method, the friction effect dominates the temperature rise. Additionally, the high temperature near the tool–chip interface could be partly attributed to element distortion. During the chip formation process of the EPSC method, the elongated elements did not fail until the critical plastic strain was satisfied. Consequently, the elements near the cutting tool experienced the worst frictional condition and the largest plastic strain, and the highest temperature was produced. Hence, the farther the distance between the zone and the cutting tool is, the lower the temperature will be.
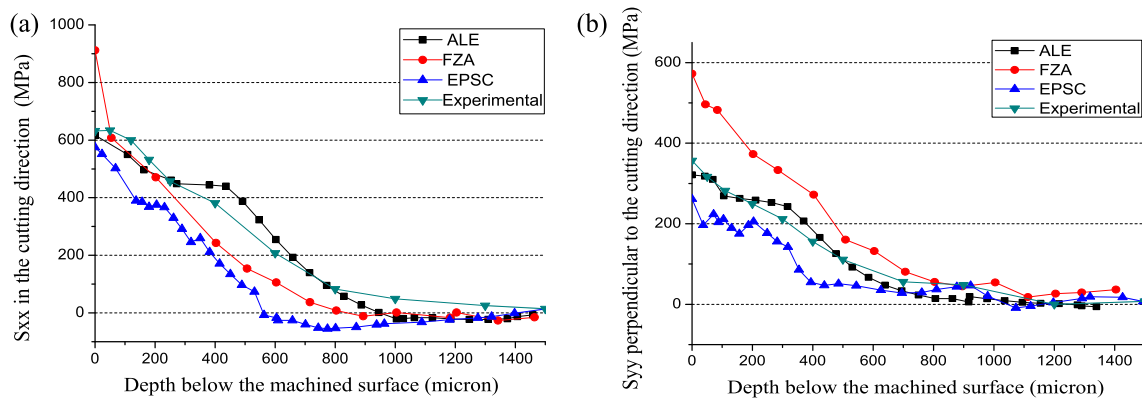
Fig. 10 Stress in the machined surface: **a** Sxx and **b** Syy; v = 70 m/min, doc = 1 mm, f = 0.15 mm/rev

4.4 Stress distribution

In the cutting experiments, residual stresses were measured by X350A X-ray diffraction which is capable of measuring surface stress in two directions X and Y, corresponding to the Sxx (along the cutting direction) and Syy (perpendicular to the cutting plane). The machined surface was electrolytically polished to determine in-depth stresses. Comparison results of the predicted stress distribution and the experimentally measured stress in the depth of machined surface are shown in Fig. 10. Both the FE predicted and experimentally measured stress values were tensile stress on the surface while the tensile stress decreased with increasing depth below the machined surface. Stress Sxx predicted by the ESPC method became compressive stress in the range of 0.6 to 1.0 mm below the machined surface, whereas the other three stress Sxx types were always tensile stress below the machined surface. Stress Sxx generated by the EPSC and FZA methods decreased rapidly compared to those of the other methods. Moreover, it can be seen that ALE produced stress Sxx that matched better with the experimentally measured stress Sxx.

Figure 10b shows the stress distribution, which is perpendicular to the cutting plane (Syy). In contrast to Sxx, the stress Syy produced by the FZA method was larger than those produced by the other methods. The stress Syy of EPSC was still the smallest of all, and this trend was consistent with stress Sxx. The measured and predicted stresses by the ALE method were in good agreement with both the magnitude and the trend.

It can be seen that the stress obtained by the four methods is tensile stress, and decreases with the increase of depth. The stress predicted by the EPSC and FZA methods decreased faster than those of the other methods. Regardless of the Sxx stress or the Syy stress, the results predicted by the ALE method were in good agreement with the experimental measurements, whether it was the stress magnitude or the trend.

5 Conclusions

In this study, a comparison of different chip formation technologies was performed to study their impacts on chip formation, cutting force, temperature, and stress distributions. Based on the current results and discussions, the following conclusions were drawn:

(1) Similar chip morphologies were generated by the ALE and FZA models. However, the chip morphology of the EPSC model was different; especially, the chip thickness predicted by the EPSC method was smaller but the chip length was longer, which was attributed to the element failure and deletion. Meanwhile, the chip thickness predicted by both the FEM and the experimentation decreased with increasing cutting speed. Moreover, the chip thickness generated by the ALE model was closer to the experimentally measured values because of the automatic material fluid during the chip formation process.

(2) Although the cutting force predicted by the FEM and experimentation decreased with increasing cutting speed, the simulated force decreased more slowly or less obviously. Additionally, the cutting force predicted by the ALE method was closest to the experimental measurement. In contrast, the other two FE models (FZA and EPSC) both produced smaller cutting forces. The deformation in the assumed failure zone in the FZA model and the inadequate use of failure parameters in the EPSC model were the primary reasons for the underestimation of the cutting force. The thrust force produced by the FZA and ALE models and by the experimentation had a similar trend at high cutting speed. The thrust force predicted by the ALE model did not show a significant reduction trend but was relatively close to the measured values, except for the low cutting speed of 15 m/min.

(3) Aside from the chip formation, the ALE and FZA methods predicted almost the same temperature distribution except for the more intensive contour lines in the ALE model. In

contrast, the EPSC method produced the highest temperature owing to the excessive element distortion. Furthermore, it appears that the temperature distributions predicted by the ALE and FZA methods were more integrated than those predicted by the ESPC method.

(4) The FZA method may not be suitable for predicting the surface stress, as the surface stress it predicted was much bigger than those predicted by the other methods. The stress predicted by the EPSC method was always small. The stresses predicted by the ALE method were more consistent with the measured stresses in terms of both stress magnitude and stress changing trend. However, it must be noted that the cutting speed is mild/moderate (15–90 m/min) in this work due to the dry condition, and it is doubtful whether the ALE method can simulate more significant chip formation of saw-tooth at high-speed.

Nomenclature FE, finite element; θ, nondimensional temperature; D_1~D_5, material-dependent fracture constants; $\Delta\overline{\varepsilon}^{pl}$, equivalent plastic strain increment; $\overline{\varepsilon}_0^{pl}$, initial equivalent plastic strain; v_f, feed rate (mm/rev); doc, depth of cut (mm); h, equivalent undeformed chip height; l', equivalent undeformed chip length; σ, flow stress; ε^{pl}, equivalent plastic strain; ε_0, strain rate parameter; $\dot{\varepsilon}^{pl}$, equivalent plastic strain rate; ε_f^{pl}, Equivalent failure plastic strain; ε^{el}, elastic strain; η_∞, η at infinite sliding velocity; η_0, η at low sliding velocity; η, non-plastic heat generation rate; γ, sensitivity to the sliding velocity; q, sensitivity to the temperature; k, heat conduction coefficient; $\partial\overline{\varepsilon}^{pl}$, effective plastic strain increment; v_c, cutting speed; θ, current temperature; θ_t, transition temperature; θ_m, melting temperature; A, JC material parameters; B, JC material parameters; C, JC material parameters; n, JC material parameters; m, JC material parameters; $\overline{F}_T$, tangential force; $\overline{F}_N$, normal force; η, friction coefficient; T, temperature parameter; η, friction coefficient; D_1~D_5, failure parameters; k, shear friction factor; ρ, density (g/mm^3); ΔT, temperature increment; ρ, density (g/mm^3); $\overline{\sigma}$, effective stress; C_p, specific heat

Author contribution Dr. Li determined the research method and experimental scheme of the paper, completed most of the finite element simulation works, and completed the writing of the paper. Master student Huang was responsible for most of the cutting experiments. Professor Liu guided the finite element simulation work of this paper. Dr. An mainly participated in the cutting simulation work of this paper, and Professor Chen provided the funding and platform for the research work of this paper.

Availability of data and materials Not applicable.

Declarations

Ethical approval Not applicable.

Consent to participate Not applicable.

Consent to publish Not applicable.

Competing interests The authors declare no competing interests.

References

1. Shaw MC (2005) Metal cutting principles, Second published. Oxford University Press, Oxford, UK 404-405
2. Hibbitt K, Karlsson BI, Sorenson P (2002) ABAQUS/explicit user's manual, ver. 6.3, HSK Inc, Providence, RI, USA
3. O¨Zel T, Zeren E (2007) Finite element modeling the influence of edge roundness on the stress and temperature fields induced by high-speed machining. Int J Adv Manuf Technol 35(3):255–267
4. Johnson GK, Cook WH (1983) A constitutive model and data for metals subjected to large strains large strain rates and high temperatures. in The 7th International Symposium on Ballistics, Hague, Netherlands
5. Haglund AJ, Kishawy HA, Rogers RJ (2008) An exploration of friction models for the chip-tool interface using an arbitrary Lagrangian-Eulerian finite element model. Wear 265:452–460
6. Barge M, Hamdi H, Rech J, Bergheau J-M (2005) Numerical modelling of orthogonal cutting: influence of numerical parameters. J Mater Process Technol 164-165:1148–1153
7. Ortiz-de-Zarate G, Sela A, Ducobu F, Saez-de-Buruaga M, Soler D, Childs THC (2019) Evaluation of different flow stress laws coupled with a physical based ductile failure criterion for the modeling of the chip formation process of Ti-6Al-4V under broaching conditions. Procedia CIRP 82:65–70
8. Tiffe M, Saelzer J, Zabel A (2019) Analysis of mechanisms for chip formation simulation of hardened steel. Procedia CIRP 82:71–76
9. Li BX, Zhang S, Zhang Q, Li LL (2019) Simulated and experimental analysis on serrated chip formation for hard milling process. J Manuf Process 44:337–348
10. Du M, Cheng Z, Wang SS (2019) Finite element modeling of friction at the tool-chip-workpiece interface in high speed machining of Ti6Al4V. Int J Mech Sci 163:105–118
11. Huang DP, Christian W, Peter W (2019) Modelling of serrated chip formation processes using the stabilized optimal transportation meshfree method. Int J Mech Sci 155:323–333
12. Chen G, Lu L, Ke ZH, Qin XD, Ren CZ (2019) Influence of constitutive models on finite element simulation of chip formation in orthogonal cutting of Ti-6Al-4V alloy. Procedia Manufacturing 33: 530–537
13. Hortig C, Svendsen B (2007) Simulation of chip formation during high-speed cutting. J Mater Process Technol 186:66–76
14. Zhang LC (1999) On the separation criteria in the simulation of orthogonal metal cutting using the finite element method. J Mater Process Technol 186:273–276
15. Rosa PAR, Kolednik O, Martins PAF, Atkins AG (2007) The transient beginning to machining and the transition to steady-state cutting. Int J Mach Tool Manu 47:1904–1915
16. Rosa PAR, Martins PAF, Atkins AG (2007) Revisiting the fundamentals of metal cutting by means of finite elements and ductile fracture mechanics. Int J Mach Tool Manu 47:607–617
17. Saez-de-Buruaga M, Esnaola JA, Aristimuno P, Soler D, Björk T, Arrazola PJ (2017) A coupled Eulerian Lagrangian model to predict fundamental rocess variables and wear rate on ferrite-pearlite steels. Procedia CIRP 58:251–256
18. Arrazola PJ, O¨zel T (2010) Investigations on the effects of friction modeling in finite element simulation of machining. Int J Mech Sci 52:31–42
19. Ducobu F, Riviere-Lorphevre E, Galindo-Fernandez M, Ayvar-Soberanis S, Arrazola PJ, Ghadbeigi H (2019) Coupled Eulerian-Lagrangian (CEL) simulation for modeling of chip formation in AA2024-T3. Procedia CIRP 82:142–147

20. Issa M, Labergere C, Saanouni K, Rassineux A (2012) Numerical prediction of thermomechanical field localization in orthogonal cutting. CIRP J Manuf Sci Technol 5:175–195

21. Zhang YC, Outeiro JC, Mabrouki T (2015) On the selection of Johnson-Cook constitutive model parameters for Ti-6Al-4V using three types of numerical models of orthogonal cutting. Procedia CIRP 31:112–117

22. Yameogo D, Haddag B, Makich H, Nouari M (2017) Prediction of the cutting forces and chip morphology when machining the Ti6Al4V alloy using a microstructural coupled model. Procedia CIRP 58:335–340

23. Courbon C, Mabrouki T, Rech J, Mazuyer D, Perrard F, D'Eramo E (2013) Towards a physical FE modelling of a dry cutting operation: influence of dynamic recrystallization when machining AISI 1045. Procedia CIRP 8:516–521

24. Nasr MNA, Ng EG, Elbestawi MA (2007) Modelling the effects of tool edge radius on residual stresses when orthogonal cutting AISI 316L. Int J Mach Tools Manuf 47(2):401–411

25. Ozel T, Llanos I, Soriano J, Arrazola P-J (2011) 3D finite element modeling of chip formation process for machining Inconel 718: comparison of FE software predictions. Mach Sci Technol 15:21–46

26. Sievert R, Noack D (2007) Simulation of thermal softening, damage and chip segmentation in a nickel super-alloy. H.K. Tonshoff, F. Hollmann (Eds.). Wiley-VCH, ISBN 527:66–76

27. Hamed E, Hamed A, Seyed MR (2021) Study on surface integrity and material removal mechanism in eco-friendly grinding of Inconel 718 using numerical and experimental investigations. Int J Adv Manuf Technol 112:1797–1818